Trace element partitioning between silicate perovskites and ultracalcic melt

Hiroshi Taura [a,1], Hisayoshi Yurimoto [b,*], Takumi Kato [c,2], Shigeho Sueno [a]

[a] *Institute of Geoscience, University of Tsukuba, Tsukuba, Ibaraki 305-8571, Japan*
[b] *Department of Earth and Planetary Sciences, Tokyo Institute of Technology, Meguro, Tokyo 152-8551, Japan*
[c] *Institute of Mineralogy, Petrology, and Economic Geology, Tohoku University, Sendai 980-8578, Japan*

Abstract

Determination of partition coefficients for Mg- and Ca-perovskite/melt has been performed for 27 trace elements by combination of high pressure–temperature experiments using a multi-anvil apparatus and in situ trace element analysis by secondary ion mass spectrometry (SIMS). Each of the crystallographic sites for the perovskites gives rise to a parabola-shaped peak on the partition coefficient versus ionic radius diagram. This suggests that the elemental partitioning is governed by the structural control even under the lower mantle condition. On the diagrams for Mg- and Ca-perovskites, sharpness and peak position of peaks are consistent with geometrical flexibility of the corresponding coordination polyhedra. The relative height between the partition curves for homovalent ions is controlled by electrostatic charge balancing among their crystallographic sites. Large partition coefficients of Th and U in Ca-perovskite suggest that these elements play an important role for the heat source in the Earth's lower mantle. © 2001 Elsevier Science B.V. All rights reserved.

1. Introduction

Understanding trace element partitioning between minerals and melts is essential in the study of magma generation in the Earth's interior. Magma is thought to be fractionated chemically by coexisting minerals. Partition coefficients of mineral/melt constrain to magma compositions. Prediction or determination of the partition coefficients of mineral/melt throughout the Earth's interior is necessary in order to constrain such chemical fractionation.

Studies of element partitioning between phenocrysts, such as olivine and pyroxenes, and magmas demonstrated the structural dependence of partition coefficients (Onuma et al., 1968; Matsui et al., 1977). The behaviors of element partitioning have been theoretically treated by elastic strain energy for substitution of host ion (Nagasawa, 1966; Blundy and Wood, 1994; Van Westrenen et al., 2000). The variation of partition coefficients is empirically controlled by the relationship between the ionic radius of the cation and the anion coordination of the mineral. The structural dependence of partition coefficients is revealed in the partitioning between olivine and melt, even at the high-pressure condition of the upper

---

* Corresponding author. Fax: +81-3-5734-2336.
E-mail address: yuri@geo.titech.ac.jp (H. Yurimoto).

mantle (Taura et al., 1998). However, the systematics of mineral/melt partitioning for minerals under the lower mantle condition are not well known.

Mg-perovskite and Ca-perovskite coexist with magma at the pressures of the lower mantle (Ito and Takahashi, 1987; Zhang and Herzberg, 1994). It is important to determine the partition coefficients between Mg-, Ca-perovskite, and silicate melts, because the partitioning behavior of these minerals constrains magma compositions in the lower mantle.

In the present study, we determine the partition coefficients of Mg- and Ca-perovskite/melt for trace elements by a high pressure–temperature (high P–T) experiment and by secondary ion mass spectrometry (SIMS). The systematics for elemental partitioning between perovskites and melt are discussed with respect to the aspect of crystal chemistry of Mg- and Ca-perovskites.

2. Experimental method

The sample used in the present study is one of the run products (run name, PVKM07) described in Kato et al. (1996). The starting material was a mixture of synthetic enstatite, group-I kimberlite and oxide dopants of La_2O_3, Ce_2O_3, Sm_2O_3, Gd_2O_3, Yb_2O_3, Sc_2O_3, ZrO_2, HfO_2, UO_2, and ThO_2 at 1000 ppm level. The mixture was processed to volatile-free glass by heating. The chemical composition is listed in Table 1. Trace elements except for dopants are introduced from the kimberlite. The sample was conditioned at 25 GPa and $2350 \pm 30°C$ for 3 min by a high P–T experiment using a multi-anvil apparatus at Tohoku University. The experimental procedure is described in detail in Kato et al. (1996). The sample was cut and polished for in situ microanalyses.

The major elements (Mg, Al, Si, Ca, Fe, and Ti) were analyzed by electron probe microanalysis (EPMA) using a JEOL 8800R at Tohoku University. The analytical results for each phase are shown in Table 1. The probe size was set to less than 5 μm in diameter for phenocrysts and set to 10–30 μm for quenched melt. The analytical conditions are described in detail in Kato et al. (1996). After the analysis, the sample surface was polished to remove the carbon coating.

The measurements for trace elements were prepared by SIMS using a modified CAMECA IMS-3f at the

Table 1
Average composition (wt.%) of each phase of run PVKM07 and the starting material

	Mg-pv	Mw	Ca-pv	Melt	Starting material[a]
SiO_2	56.80	0.90	45.20	47.80	44.95
Al_2O_3	2.00	0.40	1.90	1.60	1.79
TiO_2	1.80	0.09	2.90	2.30	1.83
Cr_2O_3	0.17	0.35	0.06	0.10	0.21
FeO	2.50	6.80	0.50	1.20	6.19
MgO	35.40	89.90	2.10	10.30	35.55
CaO	1.10	1.20	43.00	34.50	8.33
Na_2O	0.01	0.05	0.02	0.05	0.16
P_2O_5	0.00	0.00	0.45	0.75	0.99
Total	99.78	99.69	96.13	98.60	100.00
O	3	1	3		
Si	0.93	0.01	0.85		
Al	0.04	0.00	0.04		
Ti	0.09	0.13	0.15		
Cr	0.00	0.00	0.00		
Fe	0.03	0.03	0.01		
Mg	0.86	0.69	0.06		
Ca	0.02	0.01	0.86		
Na	0.00	0.00	0.00		
P	0.00	0.00	0.01		
Cation	1.97	0.86	1.97		

[a] Normalized to 100%.

Tokyo Institute of Technology. The primary ion was used as $^{16}O^-$ generated by a duoplasmatron, and the ion was accelerated to 17 keV. The primary ion beam was focused to 10–20 μm in diameter on the sample surface. The sample surface was coated with a gold film to avoid electrostatic charge-up during SIMS analysis. The positive secondary ions were detected using an electron multiplier by cycling through mass sequences in a peak-jumping mode. Secondary ions of ^7Li, ^{11}B, ^{23}Na, ^{30}Si, ^{31}P, ^{39}K, ^{45}Sc, ^{51}V, ^{52}Cr, ^{55}Mn, ^{59}Co, ^{88}Sr, ^{89}Y, ^{90}Zr, ^{93}Nb, ^{138}Ba, ^{139}La, ^{146}Nd, ^{147}Sm, ^{174}Yb, ^{180}Hf, ^{232}Th, and ^{238}U were analyzed. High-energy components of the secondary ions (90–110 eV) were collected by the energy filtering method. A glass synthesized from GSJ rock reference powder of JB-1a was used as a standard for the quantitative analysis. The JR-1 glass of GSJ rock reference was used for interference corrections of secondary ions for P and Sc detection. The analytical procedures are described in detail in Taura et al. (1998).
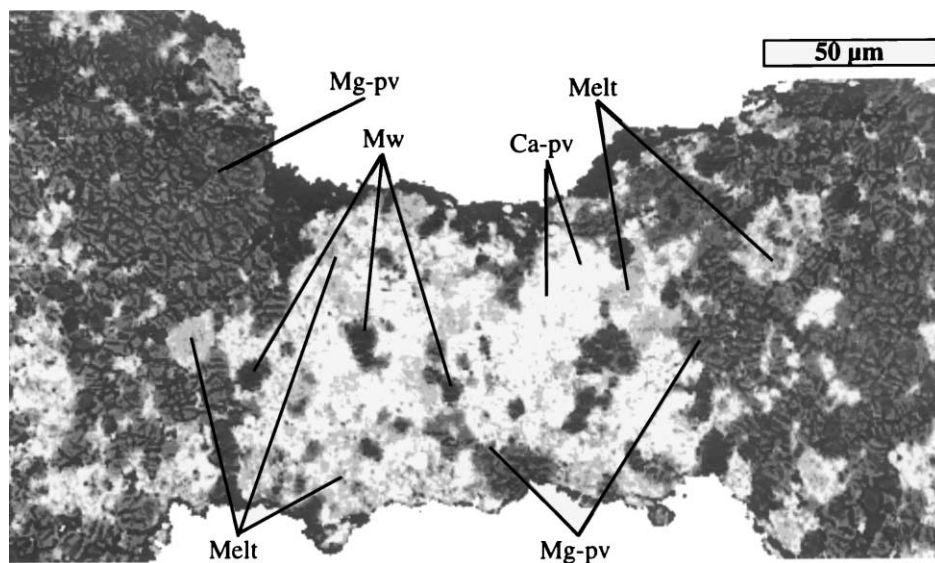
Fig. 1. Back scattered electron (BSE) image of center part of capsule of run PVKM07: Mg-pv: Mg-perovskite; Ca-pv: Ca-perovskite; Mw: magnesiowüstite; melt: quenched melt.

3. Results

The run product was composed of Mg-perovskites, Ca-perovskites, magnesiowüstites, and fine crystalline mesostasis (Fig. 1). The mesostasis should correspond to the quenched melt (Kato et al., 1996). The melt is segregated to the central portion of the capsule. Mg-perovskite crystals are enriched at both ends of the capsule. Kato et al. (1996) pointed out that the melt segregation was the result of the temperature gradient from the colder ends to the hotter center in the capsule. Although, compositions of Mg-perovskite crystals change systematically at both end parts, probably in response to temperature distribution, compositional zoning of major elements of inter- and intra-crystals for each phase was not observed in the central part of the capsule. This evidence suggests that the central part of capsule would be close to chemical equilibrium under the high P–T condition. The large melt pocket in the capsule tends to prevent the compositional change of the melt. We decided that the central part of the PVKM07 is appropriate for the examination of trace element partitioning among Mg-perovskite, Ca-perovskite, and coexisting melts.

The analytical results of trace elements for each phase are shown in Table 2. The analytical results for

major elements are more precise in EMPA than those in SIMS due to matrix effects of SIMS. On the other hand, the analytical results for trace elements are much more precise in SIMS than in EMPA due to high backgrounds of EMPA (Taura et al., 1998). Since quenched melt is composed of fine crystalline mesostasis, we used average compositions of two independent melt products in the central parts. The compositional difference between the two quenched melts is less than 30% for all elements in Table 2, except for Li and Co, the concentrations of which are below the 30 ppm level.

Mineral/melt partition coefficients for Mg, Si, Al, Ca, Ti, and Fe are calculated by the EPMA results, and those for other elements are calculated by the SIMS results. Partition coefficients, defined by the concentration ratio of crystal/melt, are shown in Table 3. For silicate perovskites, the Mg-perovskite analyzed are about 20 μm blocks, whereas Ca-perovskite crystals are composed of the aggregates of small crystals (less than 5 μm), and small amounts of quenched melt may exist in the grain boundary. The spot size of the primary beam used in the present study is small enough to analyze Mg-perovskite without contamination from surrounding phases; however, it is difficult to analyze Ca-perovskites without contamination in the quenched melt in the grain boundary. Therefore, concentration

Table 2
Concentration of each phase in the run charge[a]

	Mg-pv		Ca-pv		Melt-1		Melt-2		Average concentration (ppm)
	Concentration (ppm)	R.E.[b] (%)	Concentration (ppm)	R.E.[b] (%)	Concentration (ppm)	R.E.[b] (%)	Concentration (ppm)	R.E.[b] (%)	
Li	8.7	4	1.2	12	8.7	8	5.5	8	7.1
B	74	3	84	3	189	3	236		213
Na	<570		<390		520		610		565
Mg[c]	213000		12700		62100		62100		62100
Al[c]	10600		10100		8500		8500		8500
Si[c]	266000		211000		223000		223000		223000
P	770		590		2400		1800		2100
K	<1300		<1600		2400		2300		2350
Ca[c]	7800		307000		247000		247000		247000
Sc	1600		800		790		740		765
Ti[c]	10800		17400		13800		13800		13800
V	160	3	150	3	160	5	180	3	170
Cr	2700		1600		1700		1600		1650
Mn	920		610		880		830		855
Fe[c]	19400		3900		9300		9300		9300
Co	30	10	22	14	20	22	31	14	25.5
Sr	<450		6200		5600		4600		5100
Y	710		21400		8000		7300		7650
Zr	1500		1800		1800		1700		1750
Nb	890		600		1100	3	1200		1150
Ba	<340	3	290	4	900	4	870	3	885
La	570		13900		11000		9100		10050
Nd	220	8	9400		6600	3	5700		6150
Sm	310	7	8600		5500	3	4700		5100
Yb	580	4	9000		5100	3	5100		5100
Th	40	12	2500		1500	3	1400	3	1450
U	80	12	3600		2800	4	2200	3	2500

[a] Determined by SIMS analysis.

[b] S.D. calculated from counting statics, which is larger than 3%.

[c] Determined by EPMA analysis.

of Ca-perovskite by SIMS may be overestimated for elements of the partition coefficients that are much less than unity. The signals of Na, K, Sr, or Ba decreased gradually with sputter time for some analytical points, because these elements are enriched on the sample surface as contamination, in spite of careful treatment of the sample preparation. In the case of Mg-perovskite, although secondary ions emitted from central area of the primary beam were collected by a mechanical aperture, amounts of signals of these elements from the hollow part were not ignored. Therefore, we show the upper-limit values for these elements in Table 2.

The partition coefficients in the present study are compared with those of Kato et al. (1996) (Fig. 2). Partition coefficients for most elements are plot

systematically upward of the 1:1 line. The systematic change may be due to the difference of melt composition between them. The degree of partial melting was larger in PVKM07 than in the run charge of Kato et al. (1996), which was a lower-temperature run. The melt composition in the present study changed to Ca-poor and Mg-rich as a result of the melting of Mg-perovskite components (Table 1).

For Mg-perovskite/melt, several partition coefficients obtained in the present study are slightly different from those reported in various previous studies using mafic compositions (Kato et al., 1988a, b; Drake et al., 1993; McFarlane et al., 1994; Ohtani et al., 1995). This may be due to the compositional dependencies of partition coefficients, because in the

Table 3
Partition coefficients between Mg- and Ca-perovskites and melt

	Mg-pv/melt	R.E.[a] (%)	Ca-pv/melt	R.E.[a] (%)
Li	1.2	7	0.17	13
Be	0.35		0.39	
Na	≪1.0		0.7	
Mg	3.4		0.2	
Al	1.3		1.1	
Si	1.2		0.95	
P	0.37		0.29	
K	≪0.6		<0.7	
Ca	0.032		1.2	
Sc	2.1		1.0	
Ti	0.60		1.1	
V	1.0		0.91	
Cr	1.7		1.0	
Mn	1.1		0.71	
Fe	2.1		0.42	
Co	1.2	16	0.87	19
Sr	<0.09		1.2	
Y	0.09		2.8	
Zr	0.88		1.0	
Nb	0.76		0.52	
Ba	<0.39		0.33	5
La	0.06		1.4	
Nd	0.04	8	1.5	
Sm	0.06	7	1.7	
Yb	0.11	5	1.8	
Th	0.03	12	1.7	
U	0.03	12	1.5	

[a] S.D. calculated from counting statics, which is larger than 5%.

present study, ultra-calcic melt composition rather than mafic melt composition was prepared. Although, the variation in partition coefficients due to compositional dependence is not well known, partition coefficients in the present study are consistent with the results of Kato et al. (1996), as described above.

4. Discussion

The partition coefficients are plotted against the ionic radius of each cation, i.e. Onuma diagram (Onuma et al., 1968). The ionic radius employed the value for six-coordination at atmospheric pressure (Shannon, 1976). In the Onuma diagram, the connected curve of isovalent cations forms a parabola and the ionic radius of its peak indicates the most suitable cation size from melt to crystal (Matsui et al., 1977). The peak position would indicate how crystal
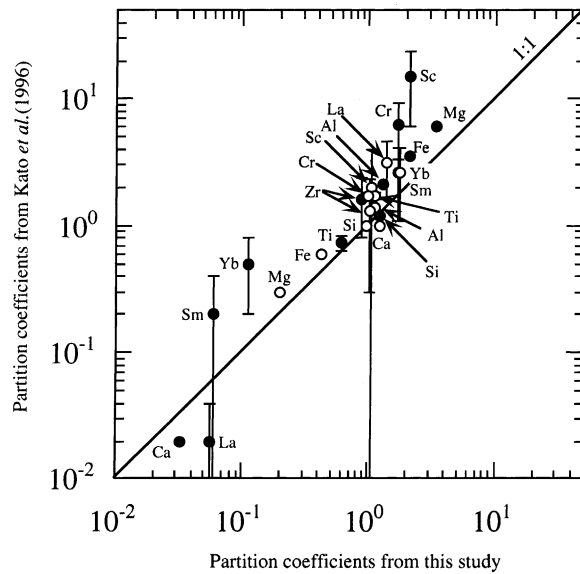

Fig. 2. Comparison of partition coefficients for Mg- and Ca-perovskite/melt between Kato et al. (1996) and the present study: (●): Mg-perovskite/melt; (○): Ca-perovskite/melt.

chemical control acts on crystal/melt partitioning for trace elements under the lower mantle condition.

4.1. Onuma diagram of Ca-perovskite/silicate melt system

The Onuma diagram of the Ca-perovskite/melt system is shown in Fig. 3. The Ca-perovskite structure
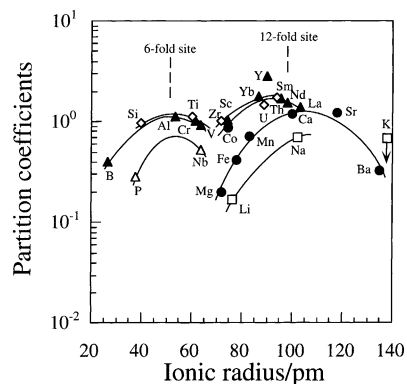

Fig. 3. Onuma diagram of Ca-perovskite/melt: (□): monovalent cation; (●): divalent cation; (▲): trivalent cation; (◇): tetravalent cation; (△): pentavalent cation.

has a cubic (*Pm3m*) symmetry (Liu and Ringwood, 1975). The stoichiometry is represented by ABO_3, which has two cation sites: A and B. The perovskite structure consists of corner-linked O octahedra. The B-cation located at center of the O octahedron, which is occupied by tetravalent cations, is primarily Si. The A-cation is arranged in the space formed by the eight octahedra. The A-site is occupied by divalent cations, mainly Ca, and is coordinated by 12 oxygen atoms and the coordination polyhedron is a regular dodecahedron.

Divalent cations of Mg, Fe, Mn, Ca, Sr, and Ba form a parabolic curve of the A-site in the Onuma diagram. The Co value is plotted upward from the divalent parabolic curve. The deviation of the Co^{2+} is thought to be due to the six-coordination preference of B-site by the crystal field stabilization energy. Plots of the Li and Na are connected parallel to the divalent curve to form a monovalent curve. The larger trivalent cations of Sc, Yb, Y, Sm, Nd, and La form a parabolic curve of the A-site. The shape of the trivalent curve is similar to that of the divalent curve, but the ionic radius of peak position is smaller than that of divalent curve. The larger tetravalent cations of Zr, U, and Th form a parallel curve to the trivalent parabolic curve of the A-site.

Parabolic curves for the B-site are formed by trivalent, tetravalent and pentavalent cations with smaller ionic radii. Trivalent cations of B, Al, V, and Cr form a parabolic curve of the B-site. Tetravalent cations of Si and Ti, and pentavalent cations of P and Nb are connected, respectively, by smooth curves that are parallel to the trivalent curve.

The peak positions of the parabolic curve of the A-site are at about 105 pm for monovalent and divalent cations, and are at about 90 pm for trivalent and tetravalent cations, respectively. The peak position of A-site for monovalent and divalent cations is larger than those for trivalent and for tetravalent cations. The variation in the peak position of A-site among isovalent curves may be explained by changing polarization of oxygen with increasing cation charge (Van Westrenen et al., 1999). The peak position of parabolic curves of the B-site is at about 50 pm, which is close to the ionic radius of Al^{3+}.

The A-site of silicate perovskite is prepared for divalent cations and the B-site is prepared for tetravalent cations. However, Table 1 shows that a considerable

amount of Al^{3+} is incorporated into the Ca-perovskite. In addition, large trivalent and tetravalent cations are also in the structure.

According to the stoichiometry, the Si^{4+} should be placed at the B-site, and the Mg^{2+}, Fe^{2+}, and Ca^{2+} should be placed at the A-site. The Al^{3+} and P^{5+} are incorporated into the B-site according to the Onuma diagram. The Ti^{4+} can be placed into the B-site as well as the A-site, because the ionic radius of Ti^{4+} is intermediate between the A- and B-peaks of the Onuma diagram. Based on these substitution rules, the composition of Ca-perovskite in Table 1 is deconvoluted as follows: $0.93(Mg^{2+}, Fe^{2+}, Ca^{2+})(Si^{4+}, Ti^{4+})O_3 + 0.04(1/4[(3Ti^{4+} + vacancy)Al_4^{3+}O_{12}]) + 0.026(1/2[(Ti^{4+} + vacancy)Ti_2^{4+}O_6]) + 0.01(1/4[(Ti^{4+} + 3 vacancy)P_4^{5+}O_{12}])$.

Since the B-site of Ca-perovskite structure prefers Al^{3+} incorporation, electrostatic charge compensation for neutralization by A-site is required. The large partition coefficients for trivalent cations shown in Fig. 3 are understood as being the result of charge compensation by the substitution of $A^{3+}Al^{3+}O_3$ (A^{3+} = large trivalent cations such as REEs and Y). The preference of REEs in Ca-perovskite may introduce fractionation of REE pattern between the upper and lower mantles.

As shown in Fig. 3, U^{4+} and Th^{4+}, which have sizes close to optimum ionic radii for the A-site, are enriched in Ca-perovskite. The enrichment of these elements plays an important role as a heat source in the Earth's lower mantle. From the Onuma diagram, the partition coefficient of Sr^{2+} and Pb^{2+} (119 pm) is approximately unity, and the partition coefficients of Rb^+ (152 pm) are estimated to be 0.1–0.01. Since these relations could produce high U/Pb and high Sr/Rb ratios, Ca-perovskite is a candidate source material for the generation of high-μ components (Zindler and Hart, 1986) of ocean island basalts.

4.2. Onuma diagram of the Mg-perovskite/silicate melt system

The Onuma diagram of the Mg-perovskite/melt system is shown in Fig. 4. Mg-perovskite structure has an orthorhombic (*Pbnm*) symmetry (Horiuchi et al., 1987) and the stoichiometry is represented by ABO_3. The orthorhombic Mg-perovskite structure can be introduced from the cubic perovskite structure of Ca-perovskite. The B-site is an octahedral site
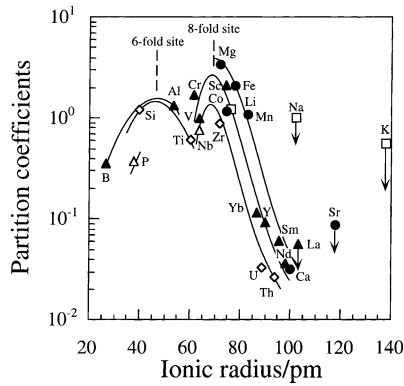
Fig. 4. Onuma diagram of Mg-perovskite/melt. Symbols are as in Fig. 3.

which is occupied by tetravalent cations, mainly Si. The A-site is occupied by divalent cations, mainly Mg. The A-site cation is coordinated by eight oxygen atoms with shorter distance and by four oxygen atoms with longer distance. Thus, the coordinated polyhedron is a distorted dodecahedron. The distortion of the dodecahedron is due to tilting of the Si-octahedra.

Divalent cations of Mg, Fe, Mn, and Ca formed a steep parabolic curve of the A-site in the Onuma diagram. The Co value is plotted downward from the divalent curve. The deviation of the Co^{2+} is thought to be due to the preference of octahedral coordination of B-site by the crystal field stabilization energy. Trivalent cations of Cr, V, Sc, Yb, Y, Sm, and Nd form a parabolic curve of the A-site, which is parallel to the divalent curve. Tetravalent cations of Ti, Zr, U, and Th also form a parallel parabolic curve of A-site. Since partition coefficients in REEs, U, and Th for Mg-perovskite are small, Mg-perovskite is not a reservoir of these elements in the lower mantle. Pentavalent cation of Nb is plotted near the tetravalent curve. Although, concentrations of Na and K in Mg-perovskite were not analyzed accurately due to surface contamination, a curve for monovalent cations may be drawn along the trivalent curve according to the plot of Li^+.

Two parabolic curves for B-site are formed by trivalent and tetravalent cations with smaller ionic radius, if the plots for isovalent cations are connected by a smooth curve and the curves are drawn parallel to each other. Pentavalent P is plotted downward from the tetravalent curve.

The Ca of the Ca-perovskite is placed in the regular dodecahedron, whereas the Mg of the Mg-perovskite is placed in the distorted dodecahedron. The distorted dodecahedra of Mg-perovskite has the large deviation of Mg–O distances (Horiuchi et al., 1987), which included the eight shorter and four longer Mg–O distances. The Mg of the Mg-perovskite is essentially coordinated by the neighboring eight O. The average eight Mg–O distance is much shorter than the Ca–O distance (Liu and Ringwood, 1975; Horiuchi et al., 1987; Hemley et al., 1987). Thus, the peak position of A-site parabola for Mg-perovskite/melt (70 pm) is significantly smaller than that of Ca-perovskite/melt (90–104 pm). The change of optimum size of A-site reflects to the different coordination in the Mg- and Ca-perovskites. The Mg is nearly optimum ion of A-site of Mg-perovskite structure.

The Si is placed in the relatively regular octahedron of the Mg-perovskite. The Mg-perovskite has a little shorter bond-length of Si–O than the Ca-perovskite (Liu and Ringwood, 1975; Horiuchi et al., 1987; Hemley et al., 1987). The peak position of B-site parabola of Mg-perovskite/melt (45 pm) is slightly smaller than that of Ca-perovskite/melt (50 pm). The difference in the optimum size of B-site parabola corresponds to the Si–O distances between Mg-perovskite and Ca-perovskite.

5. Conclusions

We reported the Onuma diagrams of Ca- and Mg-perovskites/melt based on their crystal chemistry. The two different peak positions were found to correspond to the A- and B-sites in Mg- or Ca-perovskites, respectively. The A-site peak position of Mg-perovskite is significantly smaller than that of Ca-perovskite. The distinction of peak positions resulted from the geometry of polyhedron, i.e. the A-site of Ca-perovskite is equally coordinated by 12 O, whereas that of Mg-perovskite is coordinated by neighboring eight O with short distances. The B-site peak position of Mg-perovskite is slightly smaller than that of Ca-perovskite. The different peak positions of the B-site may reflect to the Si–O bond-length of octahedron between them.

The Al^{3+} easily substitutes to B-site of Ca- and Mg-perovskite, because the ionic radius is close to

that of the B-site peak. The Al^{3+} incorporation leads to trivalent and tetravalent cations at the A-site of perovskites in order to the electrostatic charge balance. The different peak positions of A-site between Mg- and Ca-perovskites accompany the different substitution characteristics for medium- to large-sized cations. Mg-perovskite prefers middle-sized cations, such as Sc^{3+}, Zr^{4+}, and Nb^{5+}. Ca-perovskite enriches in large-sized cations, such as $REEs^{3+}$, U^{4+}, and Th^{4+}. This behavior conducts the Ca-perovskite as a heat source in the lower mantle.

Acknowledgements

References

Blundy, J., Wood, B., 1994. Prediction of crystal-melt partition coefficients from elastic moduli. Nature 372, 452–454.

Drake, M.J., McFarlane, E.A., Gasparik, T., 1993. Mg-perovskite/silicate melt and majorite garnet/silicate melt partition coefficients in the system $CaO-MgO-SiO_2$ at high temperatures and pressures. J. Geophys. Res. 98, 5427–5431.

Hemley, R.J., Jackson, M.D., Gordon, R.G., 1987. Theoretical study of the structure, lattice dynamics, and equations of state of perovskite-type $MgSiO_3$ and $CaSiO_3$. Phys. Chem. Minerals 14, 2–12.

Horiuchi, H., Ito, E., Weidner, D.J., 1987. Perovskite-type $MgSiO_3$: single-crystal X-ray diffraction study. Am. Mineral 72, 357–360.

Ito, E., Takahashi, E., 1987. Melting of peridotite under the lower mantle condition. Nature 328, 514–517.

Kato, T., Ringwood, A.E., Irifune, T., 1988a. Experimental determination of element partitioning between silicate perovskites, garnets and liquids: constraints on early differentiation of the mantle. Earth Planet. Sci. Lett. 89, 123–145.

Kato, T., Ringwood, A.E., Irifune, T., 1988b. Constraints on element partition coefficients between $MgSiO_3$ perovskite and liquid determined by direct measurements. Earth Planet. Sci. Lett. 90, 65–68.

Kato, T., Ohtani, E., Ito, Y., Onuma, K., 1996. Element partitioning between silicate perovskites and calcic ultrabasic melt. Phys. Earth Planet. Inter. 96, 201–207.

Liu, L., Ringwood, A.E., 1975. Synthesis of a perovskite-type polymorph of $CaSiO_3$. Earth Planet. Sci. Lett. 28, 209–211.

Matsui, Y., Onuma, N., Nagasawa, H., Higuchi, H., Banno, S., 1977. Crystal structure control in trace element partition between crystal and magma. Bull. Soc. Fr. Mineral Crystallogr. 100, 315–324.

McFarlane, E.A., Drake, M.J., Rubie, D.C., 1994. Element partitioning between Mg-perovskite, magnesiowüstite, and silicate melt at conditions of the Earth's mantle. Geochim. Cosmochim. Acta 58, 5161–5172.

Nagasawa, H., 1966. Trace element partition coefficient in ionic crystals. Science 152, 767–769.

Ohtani, E., Yurimoto, H., Segawa, T., Kato, T., 1995. Element partitioning between $MgSiO_3$ perovskite, magma, and molten iron: constraints for earliest processes of the Earth–Moon system. In: Yukutake, T. (Ed.), The Earth's Central Part: its Structure and Dynamics. Terrapub, Tokyo, pp. 287–300.

Onuma, N., Higuchi, H., Wakita, H., Nagasawa, H., 1968. Trace element partitioning between two pyroxenes and the host lava. Earth Planet. Sci. Lett. 5, 47–51.

Shannon, R.D., 1976. Revised effective ionic radii and systematic studies of interatomic distances in halides and chacogenides. Acta Crystallogr. A32, 751–767.

Taura, H., Yurimoto, H., Kurita, K., Sueno, S., 1998. Pressure dependence on partition coefficients for trace elements between olivine and the coexisting melts. Phys. Chem. Minerals 25, 469–484.

Van Westrenen, W., Blundy, J.D., Wood, B.J., 1999. Crystal-chemical controls on trace element partitioning between garnet and anhydrous silicate melt. Am. Mineral 84, 838–847.

Van Westrenen, W., Allan, N.L., Blundy, J.D., Purton, J.A., Wood, B.J., 2000. Atomistic simulation of trace element incorporation into garnets — comparison with experimental garnet-melt partitioning data. Geochim. Cosmochim. Acta 64, 1629–1639.

Zhang, J., Herzberg, C.T., 1994. Melting experiments on anhydrous peridotite KLB-1 from 5.0 to 22.5 GPa. J. Geophys. Res. 99, 17729–17742.

Zindler, A., Hart, S.R., 1986. Chemical geodynamics. Annu. Rev. Earth Planet. Sci. 14, 493–571.